Draft version August 8, 2023
Typeset using LaTeX default style in AASTeX631

A Search for Technosignatures Around 11,680 Stars with the Green Bank Telescope at 1.15–1.73 GHz

Jean-Luc Margot,[1,2] Megan G. Li,[1] Pavlo Pinchuk,[3] Nathan Myhrvold,[4] Lea E. Alcantara,[5] Megan T. Andrakin,[2] Jeth Arunseangroj,[2] Damien S. Baclet,[6] Madison H. Belk,[7] Zerxes R. Bhadha,[8] Nicholas W. Brandis,[9] Robert E. Carey,[7] Harrison P. Cassar,[10] Sai S. Chava,[2] Calvin Chen,[6] James Chen,[7] Kellen T. Cheng,[7] Alessia Cimbri,[2] Benjamin Cloutier,[6] Jordan A. Combitsis,[9] Kelly L. Couvrette,[11] Brandon P. Coy,[1] Kyle W. Davis,[2] Antoine F. Delcayre,[2] Michelle R. Du,[7] Sarah E. Feil,[1] Danning Fu,[2] Travis J. Gilmore,[1] Emery Grahill-Bland,[12] Laura M. Iglesias,[1] Zoe Juneau,[2] Anthony G. Karapetian,[10] George Karfakis,[7] Christopher T. Lambert,[1] Eric A. Lazbin,[7] Jian H. Li,[13] Zhuofu (Chester) Li,[2] Darren J. Lu,[10] Detao Ma,[7] Vedant Mathur,[9] Mary H. Minasyan,[2] Mark T. Nasielski,[9] Janice T. Nguyen,[2] Lorraine M. Nicholson,[2] Divij Ohri,[10] Atharva U. Padhye,[7] Supreethi V. Penmetcha,[13] Yugantar Prakash,[6] Xinyi (Cindy) Qi,[2] Vedant Sahu,[2] Joshua A. Scally,[2] Zefyr Scott,[7] Trevor J. Seddon,[2] Lara-Lynn V. Shohet,[2] Anchal Sinha,[9] Anthony E. Sinigiani,[14] Jiuxu Song,[9] Spencer M. Stice,[9] Andria Uplisashvili,[2] Krishna Vanga,[7] Amaury G. Vazquez,[2] George Vetushko,[15] Valeria Villa,[1] Maria Vincent,[1] Ian J. Waasdorp,[2] Ian B. Wagaman,[2] Amanda Wang,[10] Jade C. Wight,[1] Ella Wong,[2] Natsuko Yamaguchi,[2] Zijin Zhang,[1] Junyang Zhao,[7] and Ryan S. Lynch[16]

[1] *Department of Earth, Planetary, and Space Sciences, University of California, Los Angeles, CA 90095, USA*
[2] *Department of Physics and Astronomy, University of California, Los Angeles, CA 90095, USA*
[3] *National Renewable Energy Laboratory, Golden, CO 80401, USA*
[4] *Intellectual Ventures, 3150 139th Ave SE, Bellevue, WA 98005, USA*
[5] *UCLA Samueli School of Engineering, University of California, Los Angeles, CA 90095, USA*
[6] *Department of Mathematics, University of California, Los Angeles, CA 90095, USA*
[7] *Department of Electrical Engineering, University of California, Los Angeles, CA 90095, USA*
[8] *Department of Public Affairs, University of California, Los Angeles, CA 90095, USA*
[9] *Department of Electrical and Computer Engineering, University of California, Los Angeles, CA 90095, USA*
[10] *Department of Computer Science, University of California, Los Angeles, CA 90095, USA*
[11] *Department of Materials Engineering, University of California, Los Angeles, CA 90095, USA*
[12] *UCLA College of Letters and Science, University of California, Los Angeles, CA 90095, USA*
[13] *Department of Mechanical Engineering, University of California, Los Angeles, CA 90095, USA*
[14] *Department of Aerospace Engineering, University of California, Los Angeles, CA 90095, USA*
[15] *Department of Neuroscience, University of California, Los Angeles, CA 90095, USA*
[16] *Green Bank Observatory, P.O. Box 2, Green Bank, WV 24494, USA*

ABSTRACT

We conducted a search for narrowband radio signals over four observing sessions in 2020–2023 with the L-band receiver (1.15–1.73 GHz) of the 100 m diameter Green Bank Telescope. We pointed the telescope in the directions of 62 TESS Objects of Interest, capturing radio emissions from a total of ∼11,860 stars and planetary systems in the ∼9 arcminute beam of the telescope. All detections were either automatically rejected or visually inspected and confirmed to be of anthropogenic nature. In this work, we also quantified the end-to-end efficiency of radio SETI pipelines with a signal injection and recovery analysis. The UCLA SETI pipeline recovers 94.0% of the injected signals over the usable frequency range of the receiver and 98.7% of the injections when regions of dense RFI are excluded. In another pipeline that uses incoherent sums of 51 consecutive spectra, the recovery rate is ∼15 times smaller at ∼6%. The pipeline efficiency affects SETI search volume calculations as well as calculations of upper bounds on the number of transmitting civilizations. We developed an improved Drake Figure of Merit for SETI search volume calculations that includes the pipeline efficiency and frequency drift rate coverage. Based on our observations, we found that there is a high probability (94.0–98.7%) that fewer than ∼0.014% of stars earlier than M8 within 100 pc host a transmitter that is detectable in our search (EIRP $> 10^{12}$ W). Finally, we showed that the UCLA SETI pipeline natively detects the signals detected with AI techniques by Ma et al. (2023).

Corresponding author: Jean-Luc Margot
jlm@epss.ucla.edu

Keywords: Search for extraterrestrial intelligence - technosignatures - astrobiology — exoplanets - radio astronomy - Milky Way Galaxy

1. INTRODUCTION

In the 1982 decadal report, the Astronomy Survey Committee of the National Research Council (NRC) recommended the approval and funding of "An astronomical Search for Extraterrestrial Intelligence (SETI), supported at a modest level, undertaken as a long-term effort rather than as a short-term project, and open to the participation of the general scientific community" (National Research Council 1982). The Committee noted:

> It is hard to imagine a more exciting astronomical discovery or one that would have greater impact on human perceptions than the detection of extraterrestrial intelligence. After reviewing the arguments for and against SETI, the Committee has concluded that the time is ripe for initiating a modest program that might include a survey in the microwave region of the electromagnetic spectrum while maintaining an openness to support of other innovative studies as they are proposed.

In a subsequent report on the search for life's origins, the NRC stated: "Two parallel avenues of research should be pursued in attempts to detect life beyond the solar system: searches for evidence of biological modification of an extrasolar planet and searches for evidence of extraterrestrial technology" (National Research Council 1990). The report's recommendations included the "commencement of a systematic ground-based search through the low end of the microwave window for evidence of signals from an extraterrestrial technology".

The detection of extraterrestrial life forms is expected to usher profound developments in a wide range of scientific and cultural disciplines. These potential benefits provide compelling incentives to invest in multi-faceted searches for biological indicators (*biosignatures*) and technological indicators (*technosignatures*) of extraterrestrial life. Searches for biosignatures and technosignatures are highly complementary. In particular, the latter can "expand the search for life in the universe from primitive to complex life and from the solar neighborhood to the entire Galaxy" (Margot et al. 2019). In the Milky Way Galaxy alone, the ratio of search volumes with current and near-future technology is $V_{\rm techno}/V_{\rm bio} \gtrsim 10^6$. In terms of the number of accessible targets, the ratio is $N_{\rm techno}/N_{\rm bio} \gtrsim 10^9$.

Although some types of Solar System biosignatures (e.g., a fossil or sample organism) may offer compelling interpretations, the proposed exoplanet biosignatures are expected to yield inconclusive interpretations for some time (e.g., Fujii et al. 2018). Abiogenic interpretations may remain difficult to rule out (e.g., Rein et al. 2014), as evidenced by biosignature claims for planets that are a million times closer than the nearest exoplanet (methane on Mars, phosphine on Venus). In many cases, the spectroscopic observations may be consistent with but not diagnostic of the presence of life (e.g., Catling et al. 2018; Meadows et al. 2022). In contrast, the search for technosignatures provides an opportunity to obtain robust detections with unambiguous interpretations. An example of such a technosignature is a narrowband (say, <10 Hz at gigahertz frequencies) signal from an emitter located beyond the Solar System. Detection of a signal with these characteristics would provide sufficient evidence for the existence of another civilization because natural settings cannot generate such signals. In order to confine the signal bandwidth within 10 Hz at L band, the velocity dispersion and Doppler broadening of the species participating in the emission must remain below 2 m/s. Such coherence in velocity would have to be maintained over the physical scales of the emission sites. Fluid astrophysical settings cannot produce such conditions because the thermal velocity of species is much larger, even in the coldest environments. Even astrophysical masers cannot maintain this degree of coherence: the narrowest reported OH (1612 MHz) maser line width is 550 Hz (Cohen et al. 1987; Qiao et al. 2020), roughly two orders of magnitude wider than the proposed narrowband radio technosignatures.

Here, we describe a search for narrowband radio technosignatures around ∼11,860 stars and their planetary systems.

2. OBSERVATIONS

We observed ∼11,680 stars and their planetary systems in 62 distinct directions aligned with TESS Objects of Interest (TOIs). The characteristics of our primary targets are listed in Appendix A. To compute the number of stars captured by the 8.4 arcmin beamwidth of the telescope at 1.42 GHz, we followed Wlodarczyk-Sroka et al. (2020) and performed cone searches with the GAIA catalog (Gaia Collaboration 2023). We found 11,680 known stars, of which 8091 have measured positive parallaxes. By simple inversion of these parallaxes, we find median and mean distance estimates for these sources of 5385 ly and 18,173 ly, respectively.

We observed these stars and their planetary systems with the GBT during 2-hour sessions on 2020 April 22, 2021 April 28, 2022 May 22, and 2023 May 13. The observing cadence consisted of two scans of 150 s each per source, with sources arranged in pairs resulting in an A-B-A-B sequence for sources A and B. Angular separations between sources always exceed several telescope beamwidths. These ON-OFF-ON-OFF (or OFF-ON-OFF-ON) sequences are particularly useful in the detection of radio frequency interference (RFI) (Section 3.4).

We recorded both linear polarizations of the L-band receiver with the VEGAS backend in its baseband recording mode (Anish Roshi et al. 2012). We sampled 800 MHz of bandwidth between 1.1 and 1.9 GHz. We sampled complex (in-phase and quadrature) voltages with 8-bit quantization, but preserved only 2-bit samples after requantization with an optimal four-level sampler, which yields a quantization efficiency η_Q of 0.8825 (Kogan 1998).

3. METHODS

Our data processing techniques are generally similar to those used by Margot et al. (2018), Pinchuk et al. (2019), and Margot et al. (2021). Here, we give a brief overview and refer the reader to these other works for additional details.

3.1. *Bandpass Correction*

The VEGAS instrument splits the 800 MHz recorded bandwidth into 256 coarse channels of 3.125 MHz each. In the process of doing so, it applies a bandpass filter to each coarse channel. This filter reduces the amplitude of the baseline near both edges of the spectra. We restored an approximately flat baseline by dividing each spectrum by a model of the bandpass filter response. This model was obtained by fitting a 16-degree Chebyshev polynomial to the median bandpass response of 28 scans in the 1664.0625–1667.1875 MHz frequency range, which is generally devoid of interference because it falls in the middle of the radio astronomy protected band (1660.6–1670.0 MHz) for the hydroxyl radical. We enforced an even response by setting the odd coefficients of the polynomial to zero.

3.2. *Doppler Dechirping*

Over the 150 s duration of our scans, narrowband signals from fixed-frequency transmitters are well approximated at the receiver by linear frequency modulated (FM) "chirp" signals, where the rate of change in frequency is dictated by the orbital and rotational motions of both the emitter and the receiver. The linear FM waveform is characterized by a signal of the form

$$s(t) = A\cos(2\pi(f_0 t + Kt^2/2)), \qquad 0 \le t \le \tau, \tag{1}$$

where A is the signal amplitude, f_0 is the frequency at $t = 0$, K is the rate of change of frequency, and τ is the duration of a scan. In complex exponential notation,

$$s(t) = A\exp\left(j2\pi(f_0 t + Kt^2/2)\right) = A\exp\left(j\theta(t)\right), \qquad 0 \le t \le \tau. \tag{2}$$

The instantaneous frequency is the time derivative of the phase, i.e.,

$$f(t) = \frac{1}{2\pi}\frac{d\theta(t)}{dt} = f_0 + Kt. \tag{3}$$

The frequency increases linearly as $f(t) = f_0 + Kt$, with a total frequency excursion equal to $K\tau$. An audible signal with this time-frequency behavior would sound like a chirp, hence the name commonly attributed to the waveform.

Doppler dechirping consists of compensating for a signal's drift in time-frequency space to facilitate integration of the signal power over the scan duration. In SETI searches, the drift rate is not known a priori. We used a tree algorithm of complexity $O(N \log N)$ (Taylor 1974; Siemion et al. 2013) to integrate the signal power at 1023 trial drift rates over the range ± 8.86 Hz s^{-1} with a drift rate resolution of $\Delta\dot{f} = 0.0173$ Hz s^{-1}. This approximate technique, known as *incoherent dechirping*, does not recover 100% of the signal power. Margot et al. (2021) quantified this signal loss with a dechirping efficiency factor η_D ($0 \le \eta_D \le 1$) for a variety of settings, including searches that utilize incoherent summing of power spectra prior to signal detection. In this and previous UCLA SETI work, we do not use incoherent averaging (i.e., $N_{\text{INC\_SUMS}} = 1$) and the dechirping efficiency ranges between 60% and 100% with an average $\eta_D \simeq 72\%$ over the ± 8.86 Hz s^{-1} drift rate range. For searches with $N_{\text{INC\_SUMS}} = 51$ over a ± 4 Hz s^{-1} drift rate range (e.g., Price et al. 2020; Gajjar et al. 2021) the dechirping efficiency ranges between 4% and 100% with an average $\eta_D \simeq 16\%$. Importantly, the nominal performance of the tree algorithm for such searches is maintained in only a fairly narrow range of drift rates up to ± 0.15 Hz s^{-1}, and the efficiency drops precipitously at larger drift rates due to Doppler smearing of the signal (Margot et al. 2021, Figure 7).

The received frequency f_r of a monochromatic transmission at frequency f_t experiences a time rate of change that depends on the line of sight acceleration $\dot{v}$ between transmitter and receiver. To first order,

$$\frac{\dot{f}_r}{f_t} = \frac{\dot{v}}{c}, \tag{4}$$

where an overdot denotes a time derivative and c is the speed of light. Our selection of a range of trial drift rates with maximum value $\dot{f}_{r,\max} = \pm 8.86$ Hz s^{-1} corresponds to a fractional drift rate of ± 6.24 nHz at $f_t = 1.42$ GHz (maximum accelerations $\dot{v}_{\max}$ of 1.87 ms^{-2}). It is an appropriate choice because it accommodates line-of-sight accelerations due to the spins and orbits of most exoplanets. It can handle accelerations due the orbits of ∼73% of confirmed exoplanets with known semi-major axes and orbital periods, ∼93% of confirmed exoplanets with semi-major axes greater than 0.05 au, and 100% of confirmed exoplanets with semi-major axes greater than 0.1 au (NASA Exoplanet Archive 2019). It can also handle accelerations due to the spins of Earth-size planets at arbitrary periods (above the rotational breakup period) and Jupiter-size planets with spin periods greater than 11.5 h. Transmitters located on exotic platforms that somehow exceed these limits could escape detection by our pipeline if the transmitted waveforms were not compensated to account for the platform's acceleration (Figure 1).

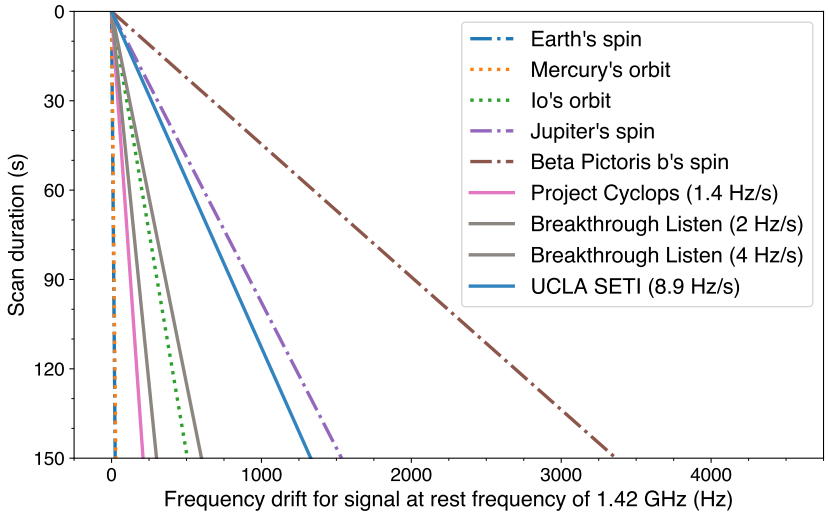

Figure 1. Expected frequency drifts from monochromatic ($f_t = 1.42$ GHz) transmitters experiencing spin and orbital accelerations in various settings. The solid lines represent the maximum drift rates corresponding to Project Cyclops, BL, and UCLA SETI searches. This figure is adapted from Sheikh et al. (2019) and reduces the drift rates sampled by BL by a factor of ∼7 to correct an error in the original figure.

3.3. *Signal Detection*

At each frequency bin, our algorithm selects the trial drift rate that yields the greatest integrated signal power and determines whether the *prominence* of the signal (Margot et al. 2021) exceeds 10 times the standard deviation of the noise. The properties of signals that exceed the threshold are stored in a structured query language (SQL) database.

In practice, the algorithm proceeds in order of decreasing prominence in each coarse channel.

3.4. *Doppler and Direction-of-origin Filters*

Signals with $\dot{f}_r = 0$ are marked as anthropogenic RFI because they imply zero line-of-sight acceleration between transmitter and receiver. Signals that are detected in more than one direction on the sky are also marked as RFI because a signal emitted beyond the Solar System can appear in only one telescope beam. Finally, sources that are detected in only one of the two scans are also marked as intermittent RFI.

The direction-of-origin filter, also known as a directional filter or sky localization filter, can be run efficiently by retrieving the signal properties from our SQL database. A more stringent filter can be obtained by running the machine learning algorithm of Pinchuk & Margot (2022).

3.5. *Visual Inspection of Remaining Signals*

Signals that remain after the line-of-sight distance and acceleration elimination process are marked as candidate technosignatures. All such candidates that fall outside of permanent RFI bands (Pinchuk et al. 2019) are visually inspected.

3.6. *Sensitivity*

The flux from a transmitter with Equivalent Isotropic Radiated Power (EIRP) at distance r is $S = \mathrm{EIRP}/(4\pi r^2)$.

The S/N of a narrowband radio link has been computed by, e.g., Friis (1946); Kraus (1986); Enriquez et al. (2017); Margot et al. (2018). It reads

$$S/N = \frac{S}{\mathrm{SEFD}}\sqrt{\frac{n_{\mathrm{pol}}\tau}{\Delta f}}, \tag{5}$$

where S is the observed flux, SEFD is the system equivalent flux density, a common measure of telescope and receiver performance, n_{pol} is the number of polarizations summed incoherently, τ is the integration time, and Δf is the channel receiver bandwidth (i.e., frequency resolution).

In a more rigorous formulation, the S/N includes the quantization efficiency η_Q due to imperfect digitization of the voltage signals and the dechirping efficiency η_D due to imperfect integration of the signal power (Margot et al. 2021):

$$S/N = \eta_Q\eta_D\frac{S}{\mathrm{SEFD}}\sqrt{\frac{n_{\mathrm{pol}}\tau}{\Delta f}}. \tag{6}$$

Quantization efficiency approaches unity with 8-bit sampling and is $\eta_Q = 88.25\%$ for an optimal two-bit sampler (Kogan 1998). Dechirping efficiency with an $\mathrm{O}(N \log N)$ algorithm depends on the frequency drift rate and ranges between 60% and 100% for the data acquisition and processing choices in this and previous UCLA SETI work, and between 4% and 100% for a BL-like process with $N_{\mathrm{INC\_SUMS}} = 51$ and $\dot{f}_r$ within ± 4 Hz s^{-1}. It is possible to improve the dechirping efficiency if one is willing to use a costly $\mathrm{O}(N^2)$ incoherent dechirping algorithm. For signals of interest with known frequency drift rates, UCLA SETI has the capability to apply a coherent dechirping algorithm to the raw voltage data, in which case $\eta_D \simeq 1$.

For the UCLA SETI program at the GBT, we have $\eta_Q = 0.8825$, SEFD = 10 Jy, $n_{\mathrm{pol}} = 2$, $\tau = 150$ s, and $\Delta f \simeq 3$ Hz. Our usual detection threshold is set at S/N=10, such that signals with flux $S_{\mathrm{det}} = 11.3 \times 10^{-26}$ W/m^2 are detectable. With these parameters, an Arecibo Planetary Radar (EIRP=2.2×10^{13} W) is detectable at 415 ly and a thousand Arecibos can be detected at 13,123 ly. Conversely, transmitters located 1000 ly away are detectable with 5.8 Arecibos and transmitters located at the galactic center are detectable with 4130 Arecibos.

3.7. *Signal Injection and Recovery Analysis*

To quantify the end-to-end efficiency of the UCLA SETI pipeline, we injected 10,000 artificial chirp signals in raw voltage data from our 2021 search, processed the data as we normally do, and quantified the number of injected signals that were recovered by the pipeline.

We used Equation (2) to inject the artificial signals in complex voltage data sampled with 8 bit quantization, and we adjusted the signal amplitudes to achieve a S/N upon recovery of approximately 20. The starting frequencies of the signals were drawn randomly from a uniform distribution in the range 1.15–1.73 GHz, with the exclusion of the 1.20–1.34 GHz range that is blocked by a notch filter at the GBT. The drift rates were drawn randomly from a uniform distribution in the range ± 8.86 Hz s^{-1} (Figure 2).

We used the exact same data files (raw voltage data files injected with 10,000 artificial signals) to estimate the end-to-end efficiency of a process that imitates the Breakthrough Listen (BL) pipeline. Specifically, we computed power spectra with the FFTW library (Frigo & Johnson 2005) and a transform length of 2^{20}, yielding a frequency resolution $\Delta f = 2.98$ Hz that approximates the finest frequency resolutions (2.79 Hz, 2.84 Hz, 2.93 Hz) of BL spectra (Lebofsky et al. 2019, Table 4). We applied a bandpass correction appropriate for the BL data acquisition backend. We then summed 51 consecutive power spectra incoherently, yielding a time resolution of 17.11 s, to approximate the 51-fold incoherent summing and time resolutions (17.40 s, 17.98 s, 18.25 s) of the High Spectral Resolution (HSR) BL spectra (Lebofsky et al. 2019, Table 4). Finally, we ran BL's version of the Doppler dechirping tree algorithm, as implemented in turboSETI (Enriquez et al. 2017), with a maximum drift rate of ± 8.88 Hz s^{-1} and minimum S/N of 10, to identify signals and quantify the number of injected signals that were recovered (`turboSETI -M 8.881784197 -s 10`).

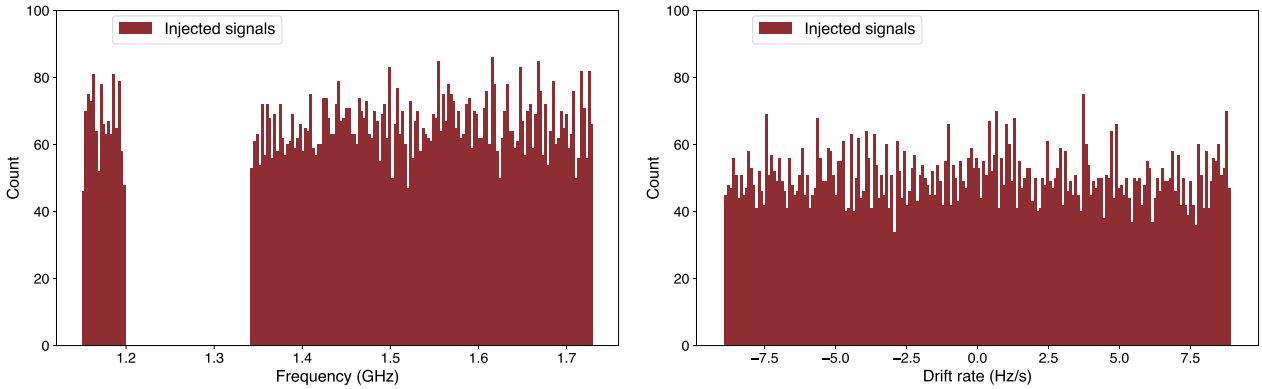

Figure 2. Distributions of starting frequencies (Left) and drift rates (Right) of 10,000 artificial, linear FM "chirp" signals injected in voltage data. Frequencies corresponding to a notch filter at the GBT (1.2 – 1.3412 GHz) are excluded.

A signal was deemed to be recovered if two conditions were jointly met: (1) the recovered frequency was within ±6 Hz of the injected frequency, and (2) the recovered drift rate was within ±0.05 Hz s^{-1} of the injected drift rate. These tolerances were designed to accommodate slight mismatches of up to two bins in the frequency dimension and the frequency drift rate dimension. The probability of an accidental match is less than 1 in a billion. Because of differences in algorithm implementation, the drift rate bins were 0.0173 Hz s^{-1} for UCLA SETI and 0.0249 Hz s^{-1} for turboSETI.

3.8. *Native Detections of Machine Learning Candidates by the UCLA SETI Pipeline*

Ma et al. (2023) used a β-convolutional variational autoencoder and random forest analysis to identify 8 promising signals not previously identified by the BL pipeline. They named these candidates MLc1 to MLc8, in reference to the machine learning (ML) process used in their analysis. We were interested in finding out whether these signals could be natively detected by the UCLA SETI pipeline, without any ML assistance. We downloaded the BL HSR power spectra of the MLc candidates and corresponding OFF scans, applied a bandpass correction (Section 3.1) appropriate for the BL data acquisition backend, and ran the resulting spectra through the UCLA SETI pipeline. We used only the first four of six scans of each pair of sources to mimic the A-B-A-B sequence used in UCLA SETI observations.

4. RESULTS

4.1. *Candidate Technosignatures*

We detected 37.1 million narrowband signals with the data from our 2020–2023 observations. Almost all (99.74%) of these signals were rejected automatically by the UCLA SETI pipeline as RFI, which left approximately 200,000 signals warranting further consideration. Tens of thousands of these signals are being inspected by thousands of volunteers on the website http://arewealone.earth as part of a citizen science collaboration (Li & Margot 2023). Almost all (99.75%) of the remaining signals were detected in regions of dense RFI. We visually inspected all ∼500 candidate technosignatures that were detected outside of dense RFI regions and determined that they were all anthropogenic.

It is remarkable that, in over 77 million narrowband signal detections obtained during an 8-year period (Table 1), not a single signal has merited follow-up observations. There have been plenty of instances where promising signals were only marginally detected in the corresponding OFF scans. We eliminate such signals from consideration.

4.2. *Signal Injection and Recovery Analysis*

The UCLA SETI pipeline recovered 9400 signals out of 10,000 injections, yielding an end-to-end pipeline efficiency for narrowband chirp signals of 94%. When regions of dense RFI were excluded, the UCLA SETI pipeline recovered 6716 signals out of 6807 injections, for an improved recovery rate of 98.7% (Figure 3). The distributions of recovered S/N and drift rates match those of the injected population (Figure 4). Signals that were not recovered are usually found near the bandpass edges, where the bandpass response and correction may be less than ideal, or intersect other signals in time-frequency space.

A process designed to imitate the BL pipeline recovered a much smaller fraction of the injections. Specifically, only 570 signals out of 10,000 injections were recovered, with S/N and drift rate distributions that do not match the injected

Data Set	Fields	Targets (primary)	Stars (in beam)	Signals (millions)	Hit Rate Density (sig kHz^{-1} hr^{-1})	DFM (GHz m^3 W$^{-3/2}$)	MDFM (Hz^2 m^3 W$^{-3/2}$)
UCLA 2016	Kepler	14	11,658	5.22	10.2	6.74e+31	3.95e+32
UCLA 2017	Kepler+	12	6,924	8.52	16.2	6.35e+31	3.72e+32
UCLA 2018–19	Gal. plane	30	25,293	27.0	24.6	1.44e+32	8.47e+32
UCLA 2020–23	TESS	62	11,680	37.1	16.4	2.99e+32	1.75e+33
Total 2016–23		118	55,555	77.8	18.0	5.74e+32	3.37e+33

Table 1. UCLA SETI search characteristics, showing observation fields, number of primary targets, number of stars observed in the beam of the telescope, number of narrowband signals detected with S/N>10, hit rate density (number of detections per unit bandwidth per unit on-source time), Drake Figure of Merit (DFM), and modified DFM (Section 5.1). Properties of all 2016–2019 detections are available online (Margot et al. 2020a,c,b).

population and illuminate the reasons for the poor performance (Figure 5). Almost all (99.1%) signals recovered by the BL-like process have drift rates within ±1 Hz s^{-1}. Injections with larger drift rates are rarely recovered. This result is entirely consistent with the theoretical expectation of low dechirping efficiency for high drift rate signals observed in incoherently summed power spectra. In this situation, the signal power gets smeared across multiple frequency resolution cells because of Doppler drift during the longer integration times. For BL incoherent sums of 51 spectra at ∼3 Hz resolution, which extend the integration times from ∼0.3 s to ∼17 s, drift rates that exceed ±0.15 Hz s^{-1} experience Doppler smearing. The dechirping efficiency falls rapidly, reaching 16% for drift rates of 1 Hz s^{-1} (Margot et al. 2021), making recovery of signals at larger drift rates challenging. The diminishing performance as a function of drift rate is evident when plotting the S/N of signals recovered by the BL-like process as a function of drift rate (Figure 6).

Detailed signal counts are listed in Table 2. These counts provide reasonable estimates of the end-to-end pipeline efficiency of radio SETI pipelines. The efficiency of a BL-like process is ∼5.7% for drift rates within ±8.88 Hz s^{-1}. Because injected signals have uniformly distributed drift rates and because all recovered signals have drift rates within the ±4 Hz s^{-1} range used by Price et al. (2020) and Gajjar et al. (2021), we can estimate the end-to-end pipeline efficiency of their searches at $5.7\% \times 8.88/4 = 12.7\%$. Likewise, we find $5.7\% \times 8.88/2 = 25.3\%$ for the work of Enriquez et al. (2017), who sampled drift rates within ±2 Hz s^{-1}.

	Number of hits prior to injection	Number of hits after injection	Candidate matches	Actual matches	Pipeline efficiency
UCLA SETI pipeline	329,591	338,238	9634	9400	94.0%
BL-like process	7512	8226	714	570	5.7%

Table 2. Efficiency of radio SETI pipelines quantified by the recovery rates of 10,000 artificial signal injections. In the UCLA SETI pipeline, a hit is defined as a narrowband signal detection with S/N ≥ 10. In the BL pipeline, a hit has the additional requirement of a minimum distance (∼ kHz) from previously recorded hits. The factor of ∼50 difference in number of hits between UCLA and BL for the same data set and drift rate range has been previously documented and is understood primarily as the result of differences in dechirping efficiency and definition of a hit (Margot et al. 2021). Because injected signals may replace one or more previously detected signals, the number of candidate matches after injection is not simply the difference in number of hits prior to and after injection. Actual matches are defined as having both a recovered frequency within ±6 Hz of the injected frequency and a drift rate within ±0.05 Hz s^{-1} of the injected drift rate. Although turboSETI in its debug mode can be coerced to reveal additional hits beyond its nominal hits, the number of actual matches in debug mode remains low at 670 recoveries out of 10,000 injections.

4.3. *Native Detections of Machine Learning Candidates by the UCLA SETI Pipeline*

The UCLA SETI pipeline successfully detected MLc3, MLc4, MLc5, MLc7, and MLc8 without invoking our own ML algorithms (Pinchuk & Margot 2022). We did not attempt to detect MLc1, MLc2, and MLc6 because the drift rates reported by Ma et al. (2023) for these signals (1.11 Hz s^{-1}, 0.44 Hz s^{-1}, 0.18 Hz s^{-1}) exceed the nominal range of the $O(N \log N)$ tree algorithm given the incoherent summing of 51 consecutive spectra in BL HSR data products.

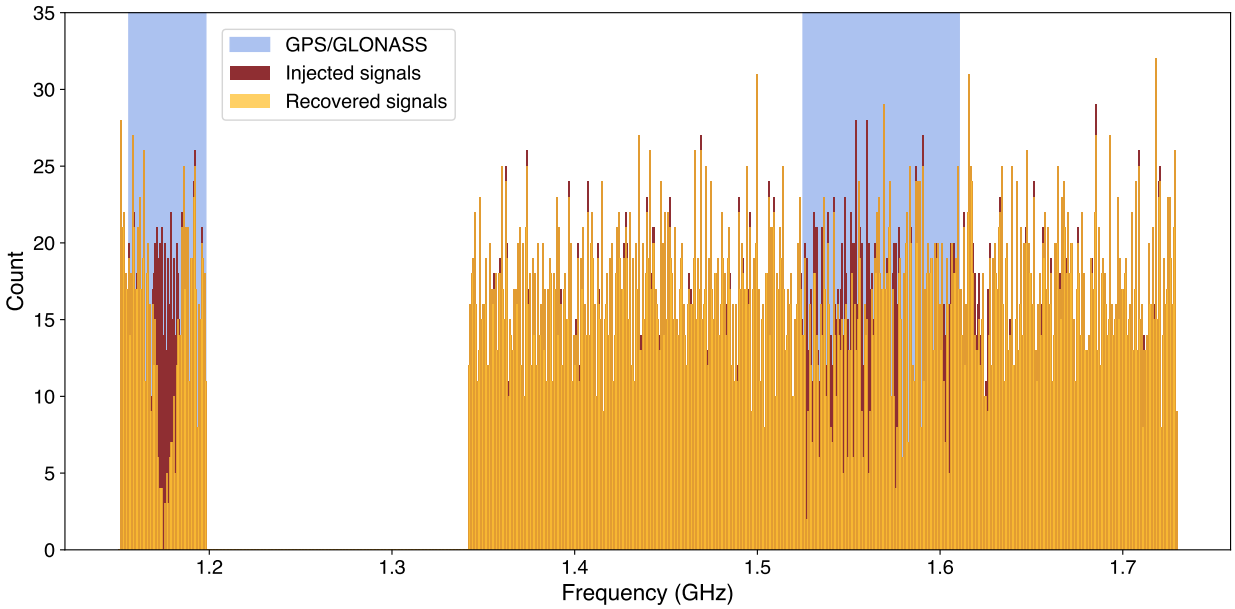

Figure 3. Distribution of injected signals and signals recovered by the UCLA SETI pipeline as a function of frequency. Blue bands indicated the operating bands of GPS and GLONASS satellites, where recovery rates are markedly lower. Frequencies corresponding to a notch filter at the GBT (1.2 – 1.3412 GHz) are excluded.

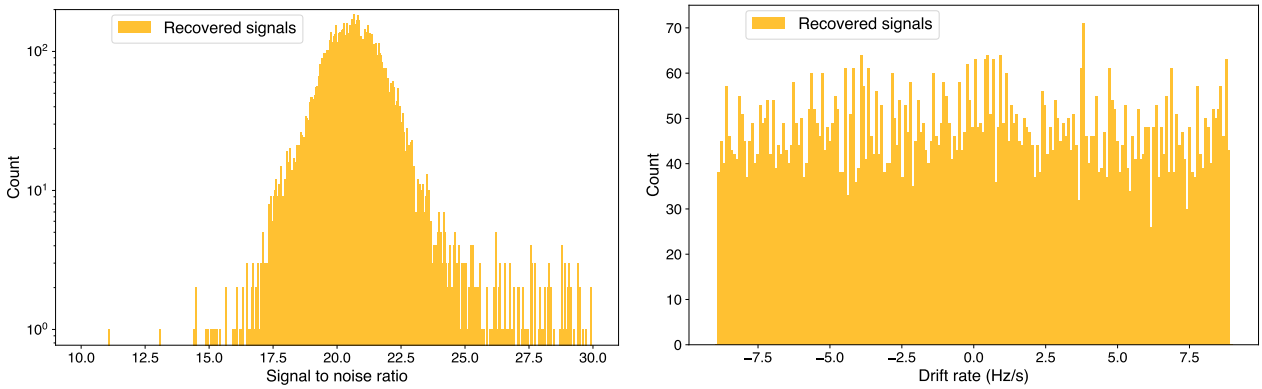

Figure 4. Distributions of recovered S/N (Left) and drift rates (Right) for the UCLA SETI pipeline.

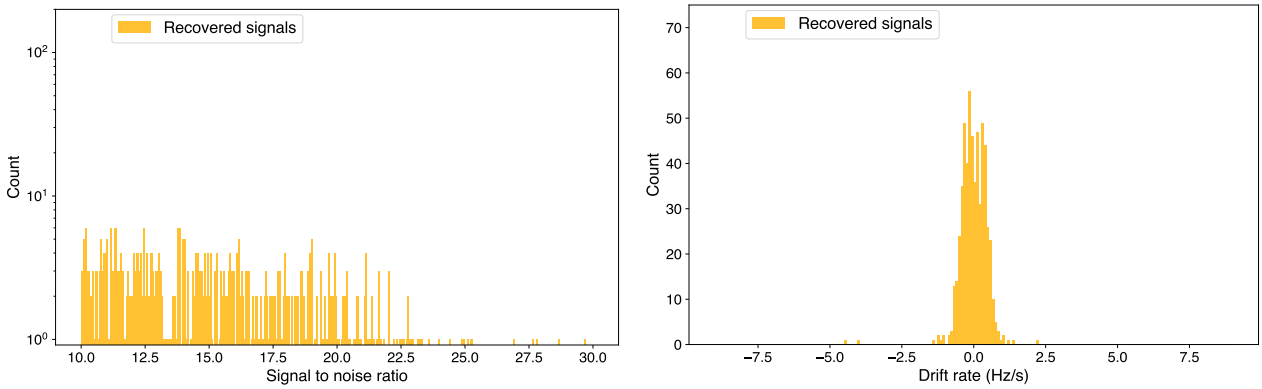

Figure 5. Distributions of recovered S/N (Left) and drift rates (Right) for a process that imitates the BL pipeline, i.e., incoherent averaging of the spectra with $N_{\text{INC\_SUMS}} = 51$ followed by signal detection with turboSETI.

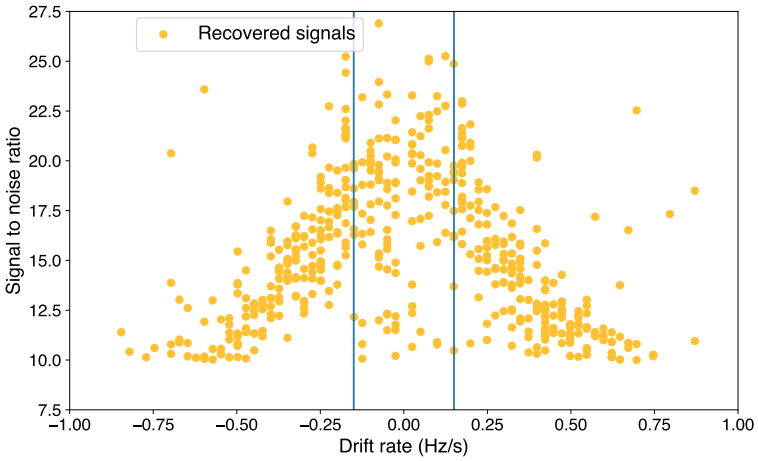

Figure 6. Distribution of recovered S/N as a function of drift rate (0–1 Hz s^{-1} only) for a process that imitates the BL pipeline. Only the central region within ±0.15 Hz s^{-1} (blue lines) is free of Doppler smearing. The recovered S/N values are lower than the injected values because of Doppler smearing that worsens at larger drift rates, as quantified by smaller dechirping efficiencies at larger drift rates. Dechirping calculations for a BL-like process had predicted a drop in S/N to about ∼62% of nominal for $df/dt = 0.25$ Hz/s, ∼31% for $df/dt = 0.5$ Hz/s, and ∼16% for $df/dt = 1$ Hz/s (Margot et al. 2021), which is roughly consistent with what is observed.

Based on the characteristics and appearance of the signals, we predict that if the raw voltage data had been preserved, we could have recovered MLc1, MLc2, and MLc6 by processing the data without incoherent summing.

The characteristics of the signals detected by the UCLA SETI pipeline generally match those of the ML detections well (Table 4.3). The magnitudes of the drift rates match, but the signs differ, which we attribute to an error in Ma et al. (2023)'s report because our values are consistent with the signal slopes in their supplemental figures.

ID	Target (HIP)	Band Freq_{Ma} (Hz)	$\text{Freq}_{\text{UCLA}}$ (Hz)	Offset (Hz)	MJD_{Ma} (days)	MJD_{UCLA} (days)	DR_{Ma} (Hz s^{-1})	DR_{UCLA} (Hz s^{-1})	S/N_{Ma}	S/N_{UCLA}
MLc1	13402	1,188,539,231	N/A	N/A	57541.68902	57541.6890	+1.11	N/A	6.53	N/A
MLc2	118212	1,347,862,244	N/A	N/A	57752.78580	57752.9095	-0.44	N/A	16.38	N/A
MLc3	62207	1,351,625,410	1,351,623,638	-1772	57543.08647	57543.1000	-0.05	+0.049	57.52	80.31
MLc4	54677	1,372,987,594	1,372,984,455	-3139	57517.08789	57517.1017	-0.11	+0.11	30.20	41.71
MLc5	54677	1,376,988,694	1,376,984,409	-4285	57517.09628	57517.1017	-0.11	+0.108	44.58	63.50
MLc6	56802	1,435,940,307	N/A	N/A	57522.13197	57522.1527	-0.18	N/A	39.61	N/A
MLc7	13402	1,487,482,046	1,487,476,704	-5342	57544.51645	57544.5977	+0.10	-0.069	129.16	113.14
MLc8	62207	1,724,972,561	1,724,970,630	-1931	57543.10165	57543.1000	-0.126	+0.138	34.09	19.85

Table 3. Characteristics of the top eight signals of interest identified by Ma et al. (2023)'s ML model and corresponding detections by the UCLA SETI pipeline. MLc1, MLc2, and MLc6 have frequency drift rates beyond the nominal range of the $O(N \log N)$ tree algorithm and we did not attempt to detect them. Columns 3, 6, 8, and 10 with subscripts "Ma" indicate the band frequency, start epoch, frequency drift rate, and S/N as reported by Ma et al. (2023). Columns 4, 5, 7, 9, and 11 with subscripts "UCLA" are corresponding UCLA SETI results. Ma et al. (2023) did not report the frequencies of the signals but rather the center frequencies of the bands in which the signals were identified. We report the actual frequencies of the signals at the beginning of each scan (column 4) and the frequency offsets (column 5) from the band centers. The modified Julian dates (MJDs) reported by Ma et al. (2023) are erroneous except for the first one. We provided the correct values (column 7). We found frequency drift rates (DR) (column 9) that are opposite in sign to those reported by Ma et al. (2023) – our values are consistent with the signal slopes in their supplemental figures. S/N values differ because of algorithmic differences in outlier rejection when computing the standard deviation of the noise.

MLc3 was detected by the UCLA SETI pipeline but correctly identified automatically as RFI because the same signal is detected in the OFF scan at S/N∼12 (Figure 7, Left).

MLc4 was detected by the UCLA SETI pipeline and identified as a candidate warranting visual inspection. Visual inspection clearly reveals the presence of the signal in the OFF scan (Figure 7, Center), indicating that this candidate is RFI.

MLc5 was detected by the UCLA SETI pipeline and identified as a candidate warranting visual inspection. Detection of the signal in the OFF scan is less compelling (Figure 7, Right), but the similarity in signal morphology with MLc4 indicates that this candidate is RFI. The frequency spacing between MLc4 and MLc5 is almost exactly 4 MHz, which suggests a common interferer.

MLc7 was detected by the UCLA SETI pipeline but correctly identified automatically as RFI because the same signal is detected in the OFF scan.

MLc8 was detected by the UCLA SETI pipeline and identified as a candidate warranting visual inspection. The signal is detected in the OFF scan and therefore labeled as RFI.

In summary, none of the MLc signals detected in our work warrant further examination.

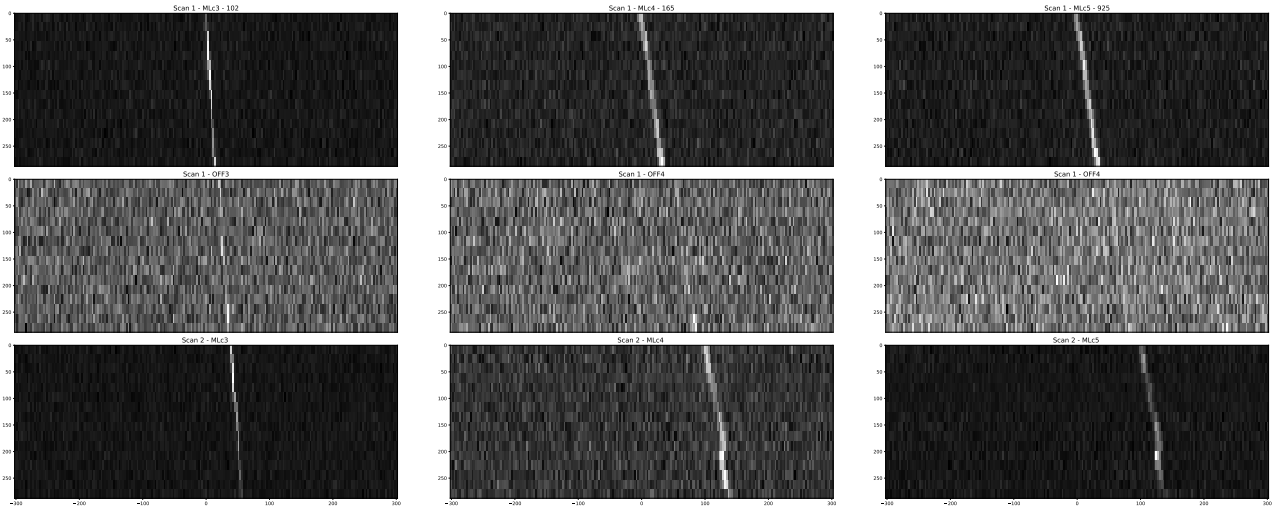

Figure 7. (Left) Dynamic spectra showing the ON-OFF-ON scans corresponding to MLc3 as detected by the UCLA SETI pipeline. The detection of the signal in the OFF scan indicates that the signal can be immediately identified as RFI. (Center) Same data for MLc4, which was identified by the UCLA SETI pipeline as a candidate worthy of visual inspection. (Right) Same data for MLc5, which was identified by the UCLA SETI pipeline as a candidate worthy of visual inspection.

5. DISCUSSION

5.1. *Figures of Merit*

The Drake Figure of Merit (Drake 1984) provides an estimate of the search volume of a SETI program that captures almost all essential elements: frequency coverage, sky coverage, and sensitivity. It is defined as

$$\mathrm{DFM} = \frac{B\,\Omega}{S_{\mathrm{det}}^{3/2}}, \tag{7}$$

where B is the total bandwidth examined, Ω is the fractional area of the sky covered, and S_{det} is the minimum flux required for a detection. Typical units are GHz m^3 W$^{-3/2}$ (e.g., Horowitz & Sagan 1993).

For transmitters of a given EIRP, the $S_{\mathrm{det}}^{-3/2}$ factor is proportional to the total volume that can be examined by a search with minimum detectable flux $S_{\mathrm{det}}(\propto \mathrm{EIRP}/4\pi r_{\mathrm{max}}^2)$. The fraction of this volume that is actually sampled by the search is proportional to the fraction Ω of a 4π solid angle. Multiple observations of the same patch of sky with similar observing parameters can easily be accounted for by rewriting $\Omega = \sum_i \Omega_i$, where the index i represents individual beam pointings. The fraction of the entire radio spectrum that is captured by the search is proportional to the bandwidth B.

In its original form, the DFM misses two essential elements. First, it assumes that pipelines are perfect with end-to-end pipeline efficiencies of 100%, whereas the efficiency of different programs can vary by more than an order of

magnitude. Second, it ignores the frequency drift rate coverage, i.e., range of line-of-sight accelerations sampled in a search, whereas this range is an obvious indicator of the thoroughness of the search. We propose a modified DFM to address these limitations:

$$\mathrm{MDFM} = \eta_P \frac{\dot{v}_{\max}}{c} \frac{B\,\Omega}{S_{\mathrm{det}}^{3/2}}, \tag{8}$$

where η_P is the end-to-end pipeline efficiency for the detection of signals of interest and $\dot{v}_{\max}/c$ is the maximum fractional frequency drift rate (with respect to the center of the band) considered in the search (Equation 4). We express the latter in nHz and show MDFM values in units of Hz^2 m^3 $\mathrm{W}^{-3/2}$. We chose a metric that is linear in the range of frequency drift rates examined because we cannot predict the locations, sizes, or spins of preferred transmitter platforms. In the absence of reliable information, a uniform prior distribution for the frequency drift rate seems reasonable. One could design the distribution to accommodate the majority of exoplanet settings, with an upper limit of 26 nHz that accommodates 95% of confirmed exoplanets with known semi-major axes and orbital periods.

Values of the DFM and MDFM metrics for the UCLA SETI search are compared to those of select surveys in Table 4 and Figure 8. We have assumed $\eta_P = 100\%$ for the surveys of Horowitz & Sagan (1993) and Harp et al. (2016) and the estimates of Section 4.2 for the surveys of Enriquez et al. (2017), Price et al. (2020), and UCLA SETI. The drift rate coverage of Horowitz & Sagan (1993) is unlike those of modern surveys. It is large but samples only three distinct values (local standard of rest, galactic barycenter, and cosmic microwave background rest frame). We have assumed a fractional drift rate of 1 nHz as a compromise, which is the same value that Harp et al. (2016) used. We found that the MDFM of the UCLA SETI search falls in between the survey of 692 stars of Enriquez et al. (2017) and the survey of 1327 stars of Price et al. (2020).

	Horowitz & Sagan 1993	Harp et al. 2016	Enriquez et al. 2017	Price et al. 2020	UCLA SETI
Freq. coverage B (GHz)	4e-4	variable[a]	0.660	variable[b]	0.439
Sky fraction Ω	0.7	1.17e-3[c]	2.88e-4	5.03e-4	4.91e-5
Sensitivity S ($\mathrm{W/m^2}$)	1700e-26[d]	260e-26[e]	17.7e-26[f]	variable[g]	11.3e-26[h]
Pipeline efficiency η_P	100%	100%	25.3%	12.7%	94.0%
Drift rate coverage (nHz)	1	1	1.33	2.66	6.24
DFM ($\mathrm{GHz\ m^3\ W^{-3/2}}$)	1.23e+31	1.70e+32	2.56e+33	2.59e+34	5.74e+32
MDFM ($\mathrm{Hz^2\ m^3\ W^{-3/2}}$)	1.23e+31	1.70e+32	8.63e+32	1.21e+34	3.37e+33

Table 4. Search volume characteristics of select surveys. The Drake Figure of Merit (DFM) does not account for pipeline efficiency nor frequency drift rate coverage, but the Modified Drake Figure of Merit (MDFM) does.

[a] We used 8 GHz for 65 stars, 2.04 GHz for 1959 stars, 0.337 GHz for 2822 stars, and 0.268 GHz for 7459 stars (Harp et al. 2016).

[b] We used 0.66 GHz for GBT L band, 0.94 GHz for GBT S band, 0.85 GHz for Parkes 10 cm (Price et al. 2020).

[c] Based on 3' × 6' synthesized beam. The solid angle appears to have been overestimated by a factor of 4 in Enriquez et al. (2017).

[d] For S/N=30 in 20 s (Horowitz & Sagan 1993).

[e] For S/N=6.5 in 93 s (Harp et al. 2016). We used a system temperature of 108 K, which is the average across all four bands.

[f] For S/N=25 in 300 s (Enriquez et al. 2017).

[g] For S/N=10 in 300 s (Price et al. 2020). We used 7.1e-26 for the GBT and 24.0e-26 for Parkes.

[h] For S/N=10 in 150 s. This values takes the quantization efficiency $\eta_Q = 0.8825$ into account.

Another possible disadvantage of the DFM is that it assumes a uniform distribution of transmitters on the sky, whereas transmitters may be preferentially located near stars, which are not uniformly distributed. At ∼1% of the galactic scale, the assumption of spatial uniformity holds reasonably well. For instance, the Gaia catalog of nearby (100 pc) stars is expected to be volume-complete for all stars of spectral type earlier than M8 and shows a roughly

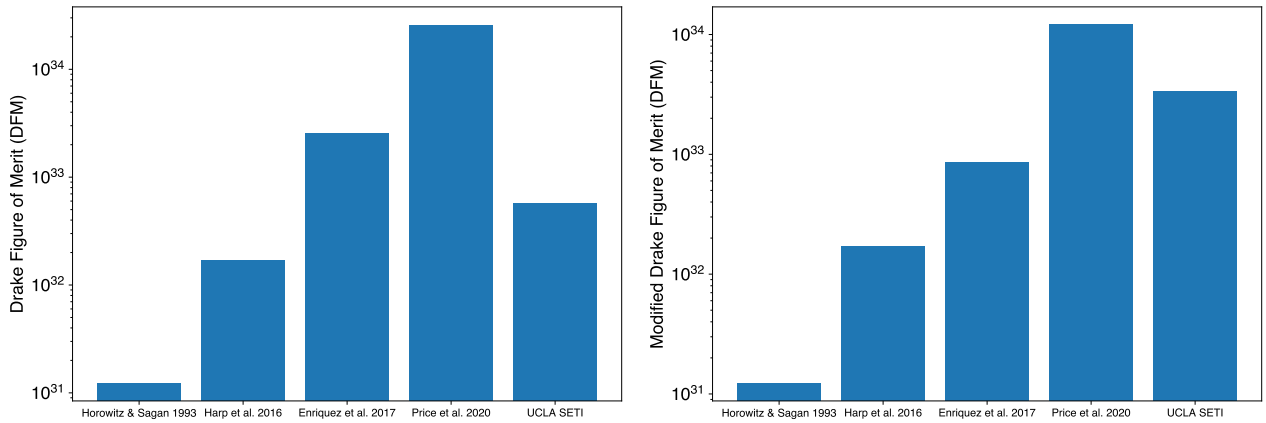

Figure 8. Search volume characteristics of select surveys. The Drake Figure of Merit (DFM, Left) does not account for pipeline efficiency nor frequency drift rate coverage, but the Modified Drake Figure of Merit (MDFM, Right) does.

uniform spatial distribution of the 331,312 objects (Gaia Collaboration et al. 2021). At larger distances, the assumption breaks down, especially for directions in and out of the plane of the galactic disk. Drake (1984) had anticipated this problem by considering distances < 1 kpc.

As our galactic models and star catalogs improve, we can refine the MDFM by replacing the physical volume covered by a search with the actual number of stars sampled by each beam pointing, assuming again that transmitters may be preferentially located near stars. Let us consider the number of stars in an elemental volume of sky

$$dN_*(r,\theta,\phi) = \rho_*(r,\theta,\phi) r^2 \sin\theta d\theta d\phi dr, \tag{9}$$

where ρ_* is a stellar density (number of stars per unit volume), and (r,θ,ϕ) describe spherical coordinates in a frame centered at the solar system barycenter. The figure of merit for transmitters of a fiducial EIRP can then be written

$$\mathrm{MDFM}|_{\mathrm{EIRP}} = \eta_P \frac{\dot{v}_{\max}}{c} B \sum_i N_{*,i} \tag{10}$$

where the number of stars in each pointing i is extracted from a catalog query that includes distance and angular bounds or computed from a galactic or extragalactic model

$$N_{*,i} = \int_o^{r_{\max}} dr \iint_{\Omega_i} \rho_*(r,\theta,\phi) r^2 \sin\theta d\theta d\phi, \tag{11}$$

with $r_{\max} = \sqrt{\mathrm{EIRP}/(4\pi S_{\mathrm{det}})}$ and Ω_i is the full width half max (FWHM) solid angle of the telescope beam. Note that the quantization and dechirping efficiencies are properly taken into account via S_{det} and, therefore, $r_{\max}$. Duplicate pointings and duplicate stars are allowed in these expressions to account for the fact that repeated observations are valuable.

5.2. *Existence Limits*

We can write a formalism to calculate upper bounds on the number of transmitters that are detectable in a SETI survey. Our calculation presupposes that transmitters are preferentially located near stars.

First, we write the total number of stars surveyed for transmitters of a fiducial EIRP

$$\mathrm{N_{obs}}|_{\mathrm{EIRP}} = \sum_i N_{*,i}, \tag{12}$$

where the number of stars is calculated as in Section 5.1. However, in this expression, duplicate stars are disallowed in the summation to avoid double-counting of stars that are observed either in duplicate pointings or in separate pointings.

Second, we write the total number of stars in the relevant search volume

$$N_{\mathrm{tot}} = \int_o^{r_{\max}} dr \iint_{\mathrm{sky}} \rho_*(r,\theta,\phi) r^2 \sin\theta d\theta d\phi, \tag{13}$$

where the double integral is over the entire sky.

Third, we acknowledge the fact that SETI pipelines are not 100% efficient. Even if we covered the entire sky in our search, the UCLA SETI pipeline would have at most a 94.0–98.7% chance of detecting a narrowband technosignature. If transmission frequencies are uniformly distributed in the range 1.15–1.73 GHz, the probability is closer to 94.0%. If the transmission frequencies happen to fall among radio astronomy protected bands or regions where RFI is less dense, the probability is closer to 98.7%.

For this survey at the fiducial EIRP of 0.058 Arecibos (1.27×10^{12} W) corresponding to detectability up to 100 pc, we find $N_{\rm obs}|_{\rm EIRP} = 47$ and $N_{\rm tot} = 331{,}312$. Therefore, we can infer with high probability (94.0–98.7%) that there are fewer than 1 star in 7,050 stars (∼0.014%) within 100 pc that host a transmitter detectable in this survey. A detectable transmitter has the following sufficient characteristics: (1) it emits in the frequency range 1.15–1.73 GHz (excluding the range 1.20–1.34 GHz), (2) it has a line-of-sight acceleration with respect to the GBT that results in a frequency drift rate within ±8.86 Hz s^{-1}, and (3) it emits a fixed-frequency or chirp waveform with bandwidth $<$ 3 Hz, EIRP $> 1.27 \times 10^{12}$ W, and 100% duty cycle. Characteristics (1) and (2) are necessary for detection, but characteristics (3) are not. For instance, we could detect more complex or broader waveforms (e.g., pulsed waveforms, non-chirp waveforms, waveforms with $>$ 3 Hz bandwidth) provided that the integrated power exceeded our detection threshold. We could also detect an intermittent transmitter provided that we observed at a favorable time.

5.3. *Revisions to Published Estimates*

Previous works (e.g., Enriquez et al. 2017; Price et al. 2020) ignored the dechirping efficiency and provided estimates of SETI search volumes or upper limits on the number of transmitters in the Galaxy under the assumption that the end-to-end efficiency of their pipeline was 100%. Our results show that the efficiency of a BL-like process is closer to 5.7% for drift rates within ±8.88 Hz s^{-1}, 12.7% for drift rates within ±4 Hz s^{-1}, and 25.3% for drift rates within ±2 Hz s^{-1}, suggesting that the published estimates of search volumes and number of transmitters in these works need revisions.

Specifically, we suggest that the statement of Enriquez et al. (2017) that "fewer than ∼0.1% of the stellar systems within 50 pc possess these types of transmitters" ought to be rephrased as "there is a 25.3% probability that fewer than ∼0.1% of the stellar systems within 50 pc possess the types of transmitters detectable in this search, which sampled frequency drift rates up to ±2 Hz s^{-1}."

6. CONCLUSIONS

Our observations of ∼11,680 stars and planetary systems with the GBT resulted in ∼37 million narrowband detections, none of which warranted reobservation.

A signal injection and recovery analysis of 10,000 chirp signals with randomly selected frequencies and drift rates revealed that the UCLA SETI pipeline recovers 94.0% of the injection and 98.7% of the injections outside of regions of dense RFI. Because the artificial signals were injected in raw voltage data, these percentages represent good estimates of the end-to-end pipeline efficiency for chirp signals.

A process that simulates the BL pipeline recovers a much smaller fraction of injections (5.7%), which we attribute largely to Doppler smearing of the signal that results from incoherent summing of 51 consecutive spectra. The characteristics of the recovered signals match the dechirping efficiency predictions of Margot et al. (2021) and confirm that the dechirping efficiency is an important factor that affects sensitivity, figure-of-merit, and transmitter prevalence calculations.

On the basis of our results and a Gaia survey of nearby (100 pc) stars that is expected to be volume-complete for spectral types earlier than M8, we can state that there is a high probability (94.0–98.7%) that fewer than ∼0.014% of such stars within 100 pc host a transmitter that is detectable in our search. Provided that the frequency and frequency drift rate fall within our search bounds, a sufficient condition for detection is the emission of a fixed-frequency or chirp waveform with bandwidth $<$ 3 Hz, EIRP $> 1.27 \times 10^{12}$ W (0.058 Arecibos), and 100% duty cycle.

We showed that the UCLA SETI pipeline can detect signals that had escaped the BL pipeline and were identified with AI techniques by Ma et al. (2023). In addition, we found that the detections were due to RFI, either because our pipeline correctly and automatically identified them as RFI, or because our usual visual inspection process showed them to be RFI.

We developed an improved Drake Figure of Merit for SETI search volume calculations that includes the pipeline efficiency and frequency drift rate coverage of a search. With this search volume metric, the UCLA SETI search to date falls in between the survey of 692 stars of Enriquez et al. (2017) and the survey of 1327 stars of Price et al. (2020).

UCLA SETI observations were designed, obtained, and analyzed by ∼130 undergraduate and ∼20 graduate students who have taken the annual SETI course since its first offering in 2016. The SETI course helps develop skills in astronomy, computer science, signal processing, statistical analysis, and telecommunications. Additional information about the course is available at https://seti.ucla.edu. UCLA SETI data are used in a citizen science collaboration called "Are we alone in the universe?", which can be found at http://arewealone.earth.

Funding for UCLA SETI was provided by The Queens Road Foundation, Robert Meadow and Carrie Menkel-Meadow, Larry Lesyna, Michael W. Thacher and Rhonda L. Rundle, Janet Marott, and other donors (https://seti.ucla.edu). We are grateful to the BL team for stimulating discussions about search modes and data processing. We thank the Tsay Family, Smadar Gilboa, Marek Grzeskowiak, and Max Kopelevich for providing an excellent computing environment in the Jim and Barbara Tsay Computer Study Lab at UCLA. We are grateful to Paul Demorest, John Ford, Ron Maddalena, Toney Minter, Karen O'Neil, and James Jackson for enabling the GBT observations. We are grateful to Norma A. Contreras, Nicholas M. Liskij, Anthony V. Lopilato, Samuel R. Mason, Maxwell K. Muller, Samantha Niemoeller, Lou Baya Ould Rouis, Taylor L. Scott, Nathanael Smith, and Nadine M. Tabucol for assistance with the data analysis. The Green Bank Observatory is a facility of the National Science Foundation operated under cooperative agreement by Associated Universities, Inc. This paper includes data collected by the TESS mission. Funding for the TESS mission is provided by the NASA's Science Mission Directorate. This work has made use of data from the European Space Agency (ESA) mission *Gaia*, processed by the *Gaia* Data Processing and Analysis Consortium (DPAC). This research has made use of the NASA Exoplanet Archive, which is operated by the California Institute of Technology, under contract with NASA under the Exoplanet Exploration Program.

Facilities: Green Bank Telescope, Exoplanet Archive

APPENDIX

A. SOURCES

TOI	Disp.	R_p ($R_\oplus$)	Period (days)	Insolation (Earth flux)	R_s ($R_\odot$)	Distance (pc)	RA (hh:mm:ss)	Dec (dd:mm:ss)
469.01	CP	3.55	13.63	60.16	1.01	68.19	06:12:13.88	-14:38:57.54
479.01	KP	12.68	2.78	615.47	1.02	194.55	06:04:21.53	-16:57:55.4
488.01	CP	1.12	1.20	58.26	0.35	27.36	08:02:22.47	03:20:13.79
536.01	KP	15.40	9.24	180.87	1.30	844.06	06:30:52.9	00:13:36.82
546.01	KP	13.44	9.20	203.95	1.12	726.41	06:48:46.71	-00:40:22.03
561.01	CP	2.74	10.78	73.35	0.84	85.80	09:52:44.44	06:12:57.97
562.01	CP	1.22	3.93	14.71	0.36	9.44	09:36:01.79	-21:39:54.23
571.01	KP	12.92	4.64	469.05	1.41	405.24	09:01:22.65	06:05:49.5
652.01	CP	2.11	3.98	464.96	1.03	45.68	09:56:29.64	-24:05:57.07
969.01	CP	3.65	1.82	167.63	0.82	77.26	07:40:32.8	02:05:54.92
1235.01	CP	1.89	3.44	134.67	0.63	39.63	10:08:52.38	69:16:35.83
1243.01	PC	4.49	4.66	8.59	0.49	43.19	09:02:55.83	71:38:11.1
1718.01	PC	4.40	5.59	219.06	0.94	52.30	07:28:04.33	30:19:18.24
1726.01	CP	2.24	7.11	145.57	0.90	22.40	07:49:55.05	27:21:47.28
1730.01	PC	2.76	6.23	114.27	0.53	35.69	07:11:27.8	48:19:40.56
1732.01	PC	2.55	4.12	38.33	0.63	74.76	07:27:12.35	53:02:42.97
1766.01	KP	16.72	2.70	1704.57	1.61	210.25	09:54:34.35	40:23:16.6
1774.01	CP	2.74	16.71	73.76	1.09	53.97	09:52:38.86	35:06:39.63
1775.01	PC	8.70	10.24	55.44	0.84	149.23	10:00:27.62	39:27:27.9
1776.01	PC	1.40	2.80	560.33	0.95	44.65	10:59:06.55	40:59:01.39
1779.01	KP	9.93	1.88	21.19	0.31	33.93	09:51:04.45	35:58:06.8
1789.01	CP	16.86	3.21	3000.05	2.26	229.07	09:30:58.42	26:32:23.98
1797.01	CP	2.99	3.65	283.72	1.05	82.34	10:51:06.41	25:38:27.83
1799.01	PC	1.63	7.09	163.47	0.96	62.13	11:08:55.9	34:18:10.85
1800.01	KP	12.42	4.12	459.54	1.26	277.28	11:25:05.98	41:01:40.87
1801.01	PC	1.99	10.64	10.73	0.55	30.68	11:42:18.14	23:01:37.32
1802.01	PC	2.51	16.80	5.92	0.58	60.69	10:57:01.28	24:52:56.42
1803.01	PC	4.22	12.89	18.34	0.69	119.24	11:52:11.07	35:10:18.48
1806.01	PC	2.84	15.15	2.15	0.40	55.52	11:04:28.36	30:27:30.87
1821.01	KP	2.43	9.49	41.92	0.77	21.56	11:14:33.04	25:42:38.15
1822.01	APC	14.57	9.61	192.62	1.71	312.52	11:11:06.68	39:31:36.02
1898.01	PC	9.17	45.52	8.34	1.61	79.67	09:38:13.27	23:32:48.29

Table 5. Characteristics of primary sources observed in 2020–2021. Columns show the TESS Object of Interest (TOI); the TESS Follow-up Observing Program Working Group disposition as of 2023 March 29 (Disp.), where PC is a planet candidate, CP is a confirmed planet, KP is a Kepler planet, and APC is an ambiguous planet candidate; the planet radius R_p in Earth radii; the orbital period in days; the insolation in Earth flux units; the radius of the host star R_s in solar radii; the distance in parsecs; and the right ascension and declination of the source.

TOI	Disp.	R_p ($R_\oplus$)	Period (days)	Insolation (Earth flux)	R_s ($R_\odot$)	Distance (pc)	RA (hh:mm:ss)	Dec (dd:mm:ss)
1683.01	PC	2.64	3.06	163.06	0.70	51.19	04:23:55.12	27:49:20.53
1685.01	CP	1.32	0.67	204.71	0.46	37.62	04:34:22.55	43:02:13.34
1693.01	CP	1.42	1.77	57.02	0.46	30.79	06:01:14	34:46:23.13
1696.01	CP	3.17	2.50	13.81	0.28	64.92	04:21:07.36	48:49:11.39
1713.01	PC	4.65	0.56	3415.83	0.95	138.37	06:42:04.94	39:50:34.45
1730.01	PC	2.76	6.23	114.27	0.53	35.69	07:11:27.8	48:19:40.56
3772.01	PC	7.32	4.17	201.89	0.87	309.14	05:44:10.44	36:04:50.35
3795.01	PC	6.47	2.83	462.81	1.01	439.84	06:34:55.79	49:40:35.67
3800.01	PC	5.74	1.67	3970.53	1.40	598.89	06:53:06.26	39:07:56.2
4596.01	PC	2.72	4.12	186.21	0.98	93.49	06:34:49.88	27:23:16.86
4604.01	KP	1.56	2.23	476.88	0.92	90.06	05:05:47.03	21:32:53.52
4610.01	PC	1.56	3.11	114.27	0.69	47.91	05:16:10.38	30:35:06.26
5087.01	KP	3.38	17.31	10.89	0.77	59.25	04:29:39.09	22:52:57.24
5129.01	PC	3.64	7.41	57.53	1.19	201.91	06:38:48.67	29:05:21.56
1459.01	PC	2.49	9.16	66.15	0.82	101.36	01:17:26.83	26:44:45.42
1468.01	CP	2.01	15.53	2.14	0.37	24.74	01:06:36.93	19:13:29.71
1471.01	PC	3.92	20.77	37.34	0.97	67.55	02:03:37.2	21:16:52.78
4511.01	PC	3.09	20.90	42.72	1.00	121.83	03:17:13.27	15:30:06.22
4524.01	CP	1.69	0.93	876.25	1.11	63.68	03:16:42.75	15:39:22.88
4548.01	PC	5.37	4.60	84.87	1.59	165.59	02:25:21.87	25:31:50.44
4607.01	PC	3.08	5.51	262.94	1.31	180.02	01:55:37.25	24:07:05.35
4637.01	PC	2.81	14.35	38.49	0.86	112.15	02:13:03.56	19:24:09.6
4639.01	PC	2.88	3.99	502.42	1.03	205.74	01:49:15.49	21:42:12.57
4649.01	PC	2.75	15.08	68.57	1.01	148.25	01:59:49.57	16:20:48.1
5076.01	PC	3.13	23.44	13.56	0.85	82.86	03:22:02.5	17:14:21.15
5084.01	PC	1.16	5.83	37.73	0.75	21.36	03:03:49.09	20:06:38.12
5319.01	PC	3.75	4.08	38.79	0.48	61.17	02:20:51.25	23:31:13.59
5343.01	PC	2.50	12.84	39.96	0.69	120.86	03:12:06.25	24:32:00.82
5358.01	PC	2.92	2.66	148.44	0.80	138.71	03:36:44.14	28:33:00.97
5553.01	PC	1.55	1.76	439.12	0.81	103.35	02:52:00.52	15:03:20.39

Table 6. Characteristics of primary sources observed in 2022–2023. Columns as in Table 5.

REFERENCES

Anish Roshi, D., Bloss, M., Brandt, P., et al. 2012, Proceedings of the XXXth URSI General Assembly in Istanbul, August 2011, arXiv:1202.0938. https://arxiv.org/abs/1202.0938

Catling, D. C., et al. 2018, Astrobiology, 18, 709, doi: 10.1089/ast.2017.1737

Cohen, R. J., et al. 1987, MNRAS, 225, 491, doi: 10.1093/mnras/225.3.491

Drake, F. 1984, SETI Science Working Group Report, ed. F. Drake, J. H. Wolfe, & C. L. Seeger, NASA Technical Paper No. TP-2244, 67–69

Enriquez, J. E., Siemion, A., Foster, G., et al. 2017, ApJ, 849, 104, doi: 10.3847/1538-4357/aa8d1b

Frigo, M., & Johnson, S. G. 2005, Proceedings of the IEEE, 93, 216

Friis, H. 1946, Proceedings of the IRE, 34, 254, doi: 10.1109/JRPROC.1946.234568

Fujii, Y., et al. 2018, Astrobiology, 18, 739, doi: 10.1089/ast.2017.1733

Gaia Collaboration. 2023, A&A, 674, A1, doi: 10.1051/0004-6361/202243940

Gaia Collaboration, Smart, R. L., Sarro, L. M., et al. 2021, A&A, 649, A6, doi: 10.1051/0004-6361/202039498

Gajjar, V., Perez, K. I., Siemion, A. P. V., et al. 2021, AJ, 162, 33, doi: 10.3847/1538-3881/abfd36

Harp, G. R., Richards, J., Tarter, J. C., et al. 2016, AJ, 152, 181, doi: 10.3847/0004-6256/152/6/181

Horowitz, P., & Sagan, C. 1993, ApJ, 415, 218, doi: 10.1086/173157

Kogan, L. 1998, Radio Science, 33, 1289, doi: 10.1029/98RS02202

Kraus, J. D. 1986, Radio Astronomy, 2nd edn. (Cygnus-Quasar Books)

Lebofsky, M., Croft, S., Siemion, A. P. V., et al. 2019, PASP, 131, 124505, doi: 10.1088/1538-3873/ab3e82

Li, M., & Margot, J.-L. 2023, in American Astronomical Society Meeting Abstracts, Vol. 55, American Astronomical Society Meeting Abstracts, 440.05

Ma, P. X., Ng, C., Rizk, L., et al. 2023, Nature Astronomy, 7, 492, doi: 10.1038/s41550-022-01872-z

Margot, J. L., Croft, S., Lazio, J., Tarter, J., & Korpela, E. 2019, BAAS, 51, 298. https://arxiv.org/abs/1903.05544

Margot, J. L., Greenberg, A. H., Pinchuk, P., et al. 2020a, Data from: A search for technosignatures from 14 planetary systems in the Kepler field with the Green Bank Telescope at 1.15–1.73 GHz, v4, Dataset, doi: 10.5068/D1309D

Margot, J. L., Pinchuk, P., Geil, R., et al. 2020b, Data from: A search for technosignatures around 31 sun-like stars with the Green Bank Telescope at 1.15–1.73 GHz, Dataset, doi: 10.5068/D1937J

Margot, J. L., Pinchuk, P., Geil, R., et al. 2021, AJ, 161, 55, doi: 10.3847/1538-3881/abcc77

Margot, J. L., Pinchuk, P., Greenberg, A. H., et al. 2020c, Data from: A search for technosignatures from TRAPPIST-1, LHS 1140, and 10 planetary systems in the Kepler field with the Green Bank Telescope at 1.15–1.73 GHz, v4, Dataset, doi: 10.5068/D1Z964

Margot, J. L., Greenberg, A. H., Pinchuk, P., et al. 2018, AJ, 155, 209, doi: 10.3847/1538-3881/aabb03

Meadows, V., et al. 2022, arXiv e-prints, arXiv:2210.14293, doi: 10.48550/arXiv.2210.14293

NASA Exoplanet Archive. 2019, Confirmed Planets Table, IPAC, doi: 10.26133/NEA1

National Research Council. 1982, Astronomy and astrophysics for the 1980's. Volume 1: Report of the Astronomy Survey Committee., Vol. 1 (Washington, DC: The National Academies Press), doi: 10.17226/549

—. 1990, The Search for Life's Origins: Progress and Future Directions in Planetary Biology and Chemical Evolution (Washington, DC: The National Academies Press), doi: 10.17226/1541

Pinchuk, P., & Margot, J. L. 2022, AJ, 163, 76, doi: 10.3847/1538-3881/ac426f

Pinchuk, P., Margot, J.-L., Greenberg, A. H., et al. 2019, AJ, 157, 122, doi: 10.3847/1538-3881/ab0105

Price, D. C., Enriquez, J. E., Brzycki, B., et al. 2020, AJ, 159, 86, doi: 10.3847/1538-3881/ab65f1

Qiao, H.-H., et al. 2020, ApJS, 247, 5, doi: 10.3847/1538-4365/ab655d

Rein, H., Fujii, Y., & Spiegel, D. S. 2014, Proceedings of the National Academy of Science, 111, 6871, doi: 10.1073/pnas.1401816111

Sheikh, S. Z., Wright, J. T., Siemion, A., & Enriquez, J. E. 2019, ApJ, 884, 14, doi: 10.3847/1538-4357/ab3fa8

Siemion, A. P. V., Demorest, P., Korpela, E., et al. 2013, ApJ, 767, 94, doi: 10.1088/0004-637X/767/1/94

Taylor, J. H. 1974, A&AS, 15, 367

Wlodarczyk-Sroka, B. S., Garrett, M. A., & Siemion, A. P. V. 2020, Monthly Notices of the Royal Astronomical Society, 498, 5720, doi: 10.1093/mnras/staa2672